frontiers | Frontiers in Earth Science

TYPE Original Research
PUBLISHED 29 August 2022
DOI 10.3389/feart.2022.939887

OPEN ACCESS

EDITED BY
Zhiwei Xu,
Nanjing University, China

REVIEWED BY
Mingrui Qiang,
South China Normal University, China
Jun Peng,
Hunan University of Science and Technology, China

*CORRESPONDENCE
Jingran Zhang,
jingranzhang@daad-alumni.de
Hao Long,
longhao@niglas.ac.cn

SPECIALTY SECTION
This article was submitted to Quaternary Science, Geomorphology and Paleoenvironment, a section of the journal Frontiers in Earth Science

RECEIVED 09 May 2022
ACCEPTED 21 July 2022
PUBLISHED 29 August 2022

CITATION
Yang N, Zhang J, Cai Y, Feng Y, Yang L, Cheng H and Long H (2022), Timing and implications of aeolian sand accumulation in a alpine basin of Qilian Shan, NE Tibetan Plateau.
Front. Earth Sci. 10:939887.
doi: 10.3389/feart.2022.939887

Timing and implications of aeolian sand accumulation in a alpine basin of Qilian Shan, NE Tibetan Plateau

Na Yang[1,2], Jingran Zhang[2,3]*, Yun Cai[1,2], Yuye Feng[1,4], Linhai Yang[5], Hongyi Cheng[6] and Hao Long[1,7,8]*

[1]State Key Laboratory of Lake Science and Environment, Nanjing Institute of Geography and Limnology, Chinese Academy of Sciences (NIGLAS), Nanjing, China, [2]School of Geography, Nanjing Normal University, Key Laboratory of Virtual Geographic Environment, Ministry of Education, Nanjing, China, [3]State Key Laboratory of Loess and Quaternary Geology, Institute of Earth Environment, CAS, Xi'an, China, [4]University of Chinese Academy of Sciences, Beijing, China, [5]School of Geography and Tourism, Shanxi Normal University, Xi'an, China, [6]College of Earth and Environmental Sciences, Lanzhou University, Lanzhou, China, [7]Qinghai Province Key Laboratory of Physical Geography and Environmental Process, College of Geographical Science, Qinghai Normal University, Xining, China, [8]Academy of Plateau Science and Sustainability, People's Government of Qinghai Province and Beijing Normal University, Xining, China

The reconstruction of regional moisture and climate changes during the Holocene has been intensively carried out over the NE Tibetan Plateau, based on different geological archives. However, owing to either the lack of robust independent chronology or ambiguous interpreting of climate proxies as well as complex geographic settings within the plateau, the nature of Holocene environmental changes and their influence factors remain controversial, particularly on whether the optimal climate condition (effective moisture peak) has prevailed during the early- or mid-Holocene. In this study, we reported a new well-dated sand dune accumulation record from the Shawotou sand field in the Babao River drainage area in the southeast Qilian Mountains, to unravel the late glacial and Holocene moisture variation history. The robust chronologies of aeolian sands and palaeosols from two sections were established based on densely collected 49 samples using post-infrared (IR) IR-stimulated luminescence dating of coarse-grained K-feldspar. Based on stratigraphic investigation of the sand dune/palaeosol sections, the results show that the climatic condition was very dry during the late glacial and early Holocene (14–8 ka), characterized by sand dune formation, and then the moisture peaked in the middle Holocene (8–4 ka) with the strongest pedogenesis, followed by a relatively dry condition in the late Holocene (since 4 ka). The regional comparison suggested that the Holocene moisture variation pattern seems synchronous over the NE Tibetan Plateau, that is, the dry early Holocene and late Holocene but with peaked moisture in the middle Holocene, which is likely attributed to the precipitation changes of the East Asian summer monsoon.

KEYWORDS

paleoclimate, Holocene, sand-palaeosol sequence, Northeastern Tibetan Plateau, luminescence dating

1 Introduction

Known as the Third Pole of the world, the Tibetan Plateau (TP) is very sensitive to global climate change and has long been the hotspot in the study of regional and global environmental change (An et al., 2000; Bond et al., 2001; Mayewski et al., 2004). The Holocene epoch (~12 ka to now) is a key period for the rapid development of human society, which also provides an ideal scene for studying the pattern of climate change in geological history and predicting the evolution trend of the human living environment in the future (Chen et al., 2016). As a unique geographical unit, the northeast TP (NETP) is jointly affected by the Asian monsoons and westerly circulation (An et al., 2012). At present, there is still a great discrepancy in the understanding of the Holocene environmental changes in this region, especially the evolution history of moisture conditions (Chen et al., 2016).

Regarding the Holocene moisture variation pattern in the NETP, one major point of view has put forward a dry early Holocene with strong dust activity and regional environmental drought, a wet mid-Holocene, and a relatively wet late Holocene. For instance, luminescence ages of aeolian sand and loess strata in the Qinghai Lake Basin show that strong dust activity and aeolian sand accumulation mainly occurred in the early Holocene, indicating very low regional effective humidity during this time (Lu et al., 2011; ChongYi et al., 2019; Liu et al., 2019; Zhang et al., 2022). Stauch (2015) integrated and analyzed the aeolian sedimentary records in the NETP, and concluded that strong aeolian activities prevailed in the early Holocene with the dry regional climate, while the aeolian activity weakened in the middle Holocene (7–3.6 ka) accompanied by humid climate conditions. This has further been confirmed in the study by Chen et al. (2016), who evaluated the paleoclimatic significance of different sediment carriers and indicators from Qinghai Lake, and suggested that the NETP has undergone the wettest stage in the middle Holocene. In contrast, many proxy records of lake sediments, for example, ostracod shell isotopes (Lister et al., 1991; Wei and Gasse, 1999; An et al., 2012), leaf wax hydrogen isotopes (Thomas et al., 2016), carbonate and organic matter content (An et al., 2012; Liu et al., 2014), and element geochemical index Rb/Sr (Jin et al., 2015), demonstrated that the strongest monsoon-induced wettest climate conditions occurred in the early Holocene in the NETP, while the climate condition deteriorated toward the middle and late Holocene. According to the previous studies mentioned earlier, the Holocene climate and moisture variation pattern of NETP can be summarized in two views: one is that the regional climate was humid in the early Holocene (11–7 ka) and relatively dry in the middle and late Holocene, mostly based on lake core sediments; the other one is that the climate was humid in the middle Holocene (7–3.5 ka) but relatively dry in the early Holocene and late Holocene with strong aeolian activities. Thus, more robust records are required to reconcile the contentious issue of whether an optimal climate condition (effective moisture) prevailed during either the early- or mid-Holocene.

It should be noted that most lake records from NETP were based on ^{14}C dating of bulk organic carbon, which may have suffered from some problems in age controls of lake sediments from the arid and cold regions (Long et al., 2011; Hou et al., 2012; Mischke et al., 2013). For bulk organic matter in lake sediments, the major uncertainty of ^{14}C dating is the contamination by older carbon from the catchment (i.e., reservoir effect). It has been revealed that the reservoir effects can be spatially and temporally variable from one lake to another and also through geological time even for the same sedimentary sequence (Long et al., 2015), which could further affect the results of the Holocene environmental reconstruction based on lake sedimentary records. On the other hand, due to the complexity of the depositional processes in lakes, multiple or even contradictory interpretations of climatic proxies existed (Liu et al., 2008; Long et al., 2012). In contrast, sand dune sediments from arid and semiarid areas have a more straightforward indication of the past moisture variations, for example, the aeolian sand/palaeosol stratigraphy can be clearly indicative of regional aridity/wetness, and its chronological framework is easy to be established accurately based on optically stimulated luminescence dating techniques (Lu et al., 2011; Long et al., 2017; Yang et al., 2019; Kang et al., 2020; Li et al., 2020). It should be aware that high-resolution sampling and dating strategy is of crucial importance for studying the aeolian sediments, for the fragmentary and low-resolution chronological frameworks may have difficulties in obtaining a full picture of aeolian activities and further cause possible misinterpretation of the paleoenvironment implications (Telfer and Thomas, 2007; Long et al., 2016).

In this study, we present a new sand dune accumulation record from the Babao River drainage in the southeast of the Qilian Mountains (Figure 1A). We conduct high-resolution post-IR IRSL dating of K-feldspar to set up the chronological framework of two aeolian sand and palaeosol sequences to reconstruct the aeolian accumulation history and infer the Holocene moisture changes in the NETP. The results are compared with other Holocene hydroclimate records from adjacent areas, and the potential controlling factors of Holocene aeolian activity in the NETP are discussed.

2 Study area and materials

Babao River (Figure 1B) is the eastern upper reach of the Heihe River, which originates from the high mountain areas and flows into the Hexi Corridor. In the Babao River drainage area, the annual mean temperature is 2.4°C, and the annual mean precipitation and potential evaporation are 400 and 780 mm, respectively (Niu and An, 2013). The modern climate of the area is mainly affected by the East Asian monsoon and the mid-

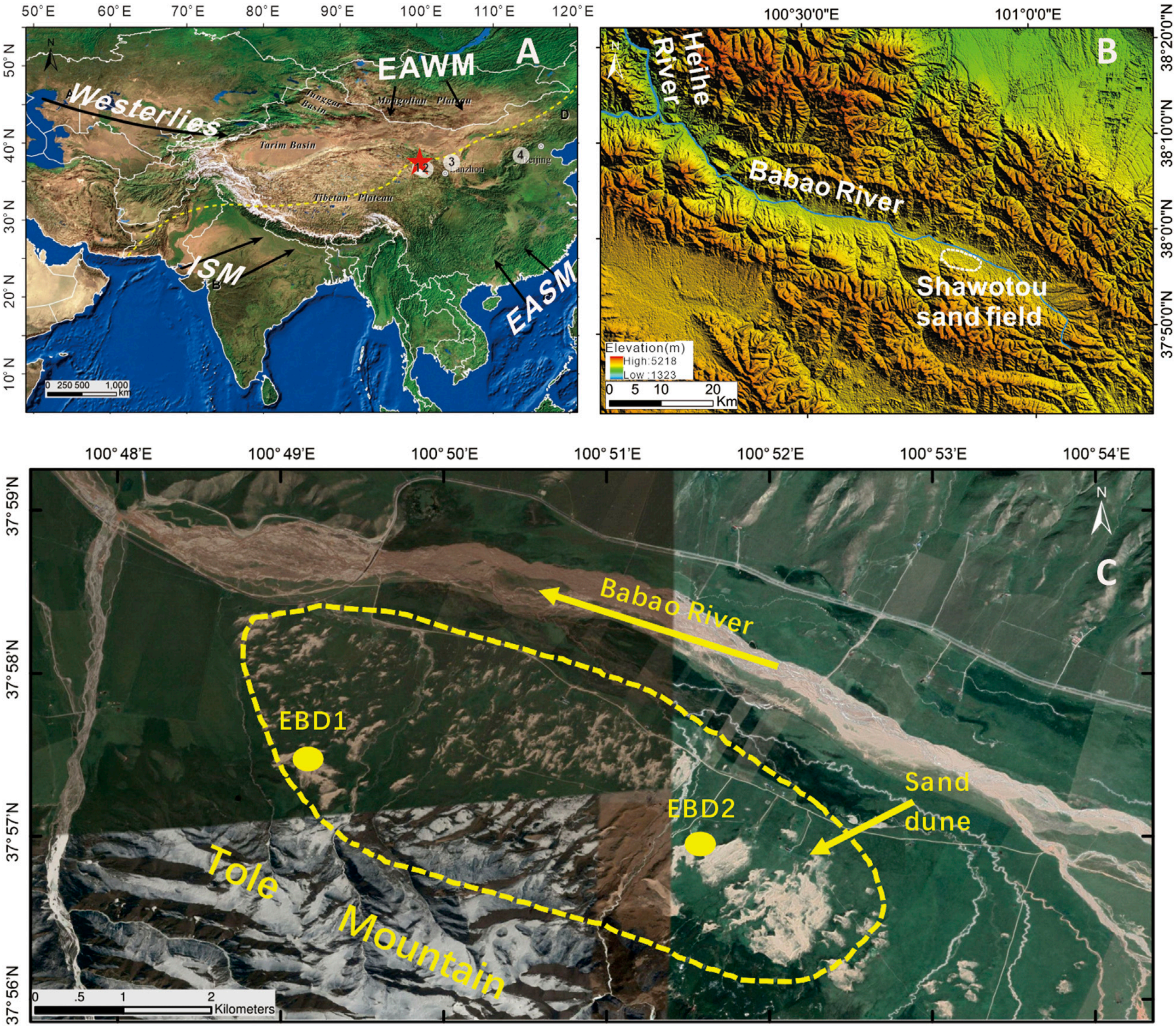

FIGURE 1
(A) Location of the study area (red star) and the main atmospheric circulation systems influencing the area, such as westerlies, EASM, and EAWM. The figures denote the paleoclimate records discussed in the text: ① Qinghai Lake (Li et al., 2017), ② Dalianhai in Gonghe basin (Cheng et al., 2013), ③ Baijian Lake basin (Long et al., 2012), and ④ Gonghai Lake (Chen et al., 2015); **(B)** DEM of the Babao River drainage area in southeast Qilian Mountains; locality of the Shawotou sand field near Ebao Town is outlined; **(C)** the satellite image of the Shawotou sand field and solid yellow dots are the sites of two sections.

latitude westerly wind, resulting in a continental alpine mountain climate. The vegetation types are mainly characterized by alpine meadow, subalpine shrub, and alpine grassland.

Along the south bank of the Babao River close to the Ebao Town, a dune field called Shawotou (37°57′-37°58′N, 100°48′-100°53′E, Figure 1B) is developed, covering an area with a width of 2–3 km from north to south and length of 10–12 km from east to west. The dune landforms can be identified from aerial photos (Figure 1C), showing that these dunes are undergoing erosion. It used to be pasture having a good vegetation cover. However, overgrazing, deforestation, and grassland reclamation have caused land degradation since the 1950s, resulting in vegetation destruction and palaeodunes exposure in large areas (Cheng et al., 2014). Many aeolian sand/palaeosol strata have been exposed (Figure 2). We excavated two sand and palaeosol sections named EBD1 (the top half of Figure 2) and EBD2 (the lower half of Figure 2) in the middle and west of the dune field, both of which were not bottomed (inset of Figure 2). To reach further down to the bottom of the dune sand, a 2-m-long sedimentary core was drilled at the bottom of the

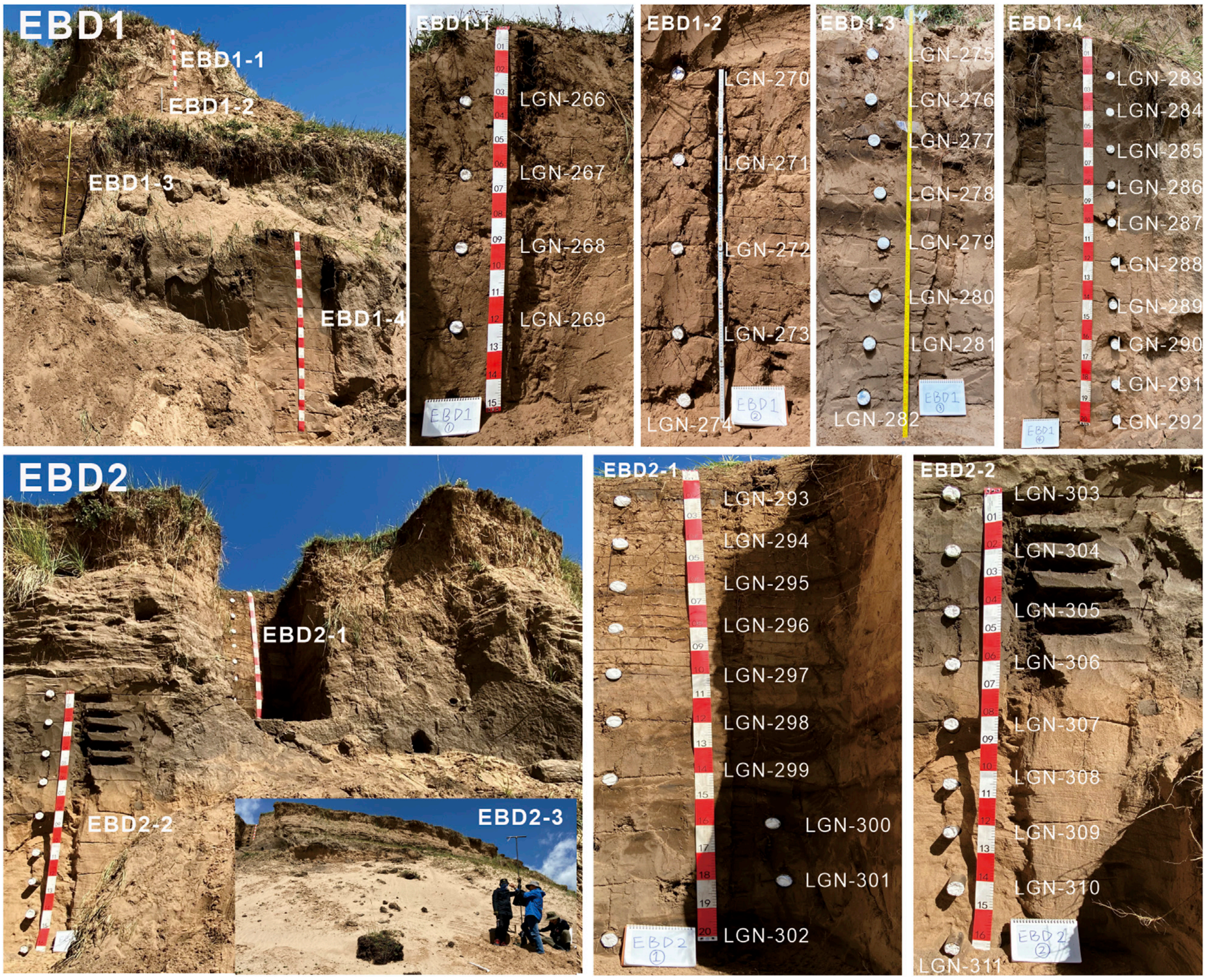

FIGURE 2
Overview and sedimentary variation photographs of two stacked aeolian sand palaeosol sequences.

EBD2 section. Howbeit, the base of the dune sand has not been reached.

The two sections are overall stratigraphically consistent with each other, which can be divided into six stratigraphic units (Figure 3), based on changes in bedding, color, and texture from bottom to top. The lowermost unit (U1) mainly consists of yellowish and well-sorted sand without any signs of pedogenesis; U2 consists of yellowish consolidated silty sand, which is indicative of the strengthening pedogenic process and transition from dune sand to palaeosol; this transitional layer is covered by a typical palaeosol unit (U3) composed of major fine-grained sand and amount of coarse silt, showing the strongest pedogenic intensity in the entire sequence; U4 is another transition layer mainly composed of yellowish consolidated silty sand. It is noteworthy that for the EBD1 section, on top of this transition layer, there is a weakly developed soil layer consisting of gray sandy silts and intercalated by fine to medium silts with centimeter-scale horizontal and sub-horizontal bedding; U5 mainly consists of sand or silty sand, and the upper part (U6) is modern surface soil containing plant roots.

A total of 49 samples were densely collected for luminescence dating, 46 of which were sampled by hammering the steel cylinder (5 cm in diameter and 20 cm in length) into the newly cleaned section wall at a 20- to 30-cm interval. The filled cylinders were sealed with aluminum foil to avoid light exposure and water loss. Three samples were collected from the drill core at a 0.5-m interval at the bottom of the EBD2 section.

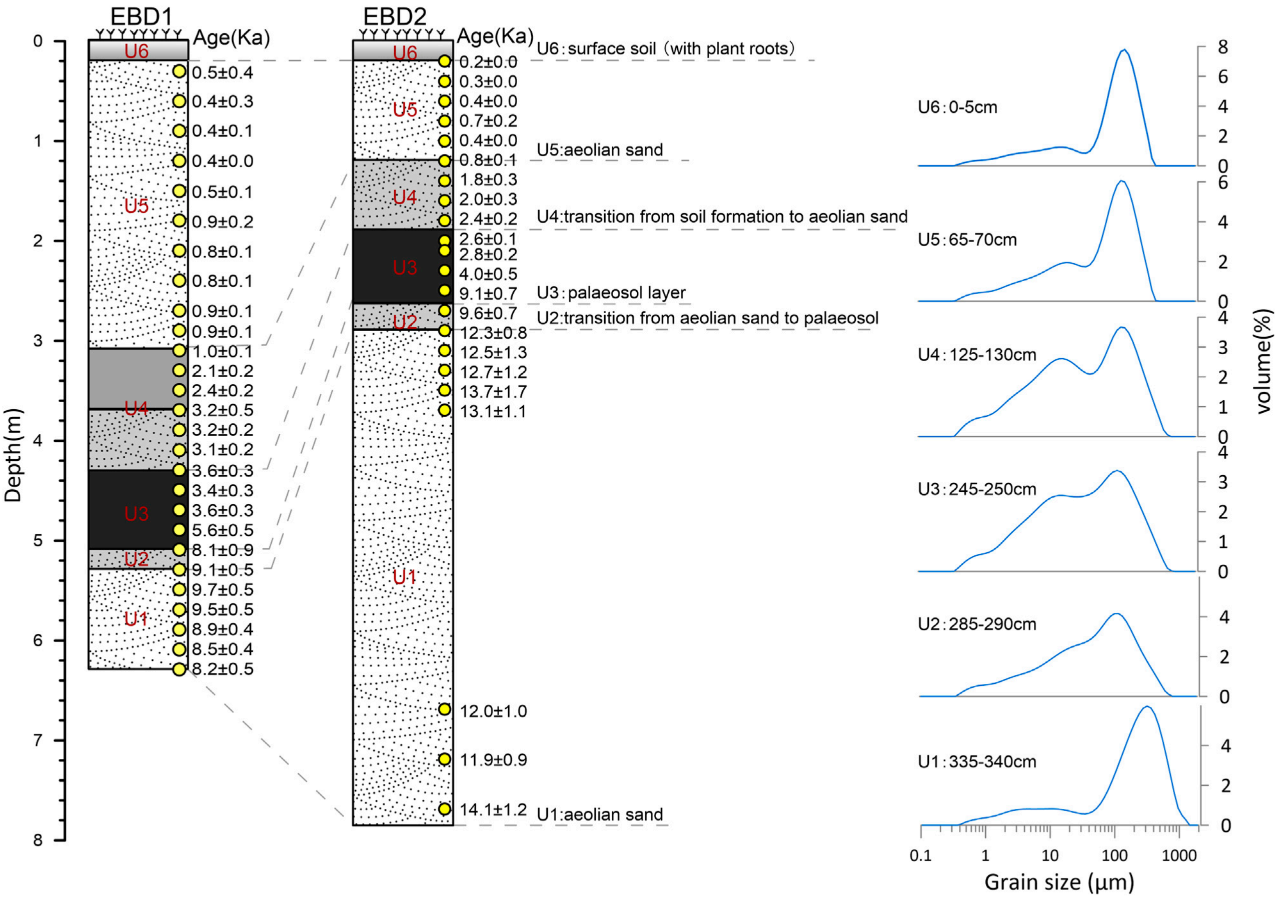

FIGURE 3
Stratigraphy and chronology of the EBD1 and EBD2 sections and typical grain size distribution frequency curves of each of six layers.

3 Methods and facilities

3.1 Sample preparation and equipment for luminescence dating

Luminescence dating was carried out at the Luminescence dating laboratory, School of Geography, Nanjing Normal University (LGN). Sediments from both ends of the cylinder were scraped out for dose rate determination. The samples in the middle were wet sieved to obtain coarse grain (CG) fraction with grain size between 100 and 200 μm. The CG fraction was then treated with 10% HCl and 30% H_2O_2 to remove carbonate and organic matter, respectively. Subsequently, the K-feldspar-rich grains (< 2.58 g/cm^3) were density separated using sodium polytungstate. Finally, the K-feldspar-rich grains were stuck monolayered onto the steel discs with an area of ~2 mm using silicon spray.

All D_e measurements were conducted on an automated Risø TL/OSL-20 reader equipped with a ^{90}Sr β source (dose rate was 0.093 Gy/s at the time of measurement). The infrared-stimulated luminescence (IRSL) signal of K-feldspar minerals was stimulated by IR LEDs (870 nm) and detected by a photomultiplier tube through a combination of Schott BG-39 and BG-3 filters in the blue light spectrum between 320 and 450 nm.

3.2 D_e determination and dose rate calculation

The post-IR IRSL (pIRIR) protocol was applied to the K-feldspar D_e determination (Buylaert et al., 2009). In order to test the temperature dependency of the pIRIR D_es, a series of D_es were measured under five sets of measurement conditions (different preheat and pIRIR stimulation temperature combinations) using sample LGN-304. Preheat temperature was set at 180, 200, 250, and 320°C, followed by the first IRSL fixed at 50°C for 120 s (IR_{50}). The second IRSL, which is the pIRIR signal, was stimulated for 120 s at an elevated temperature that tracked the preheat temperature by −30°C, except that for

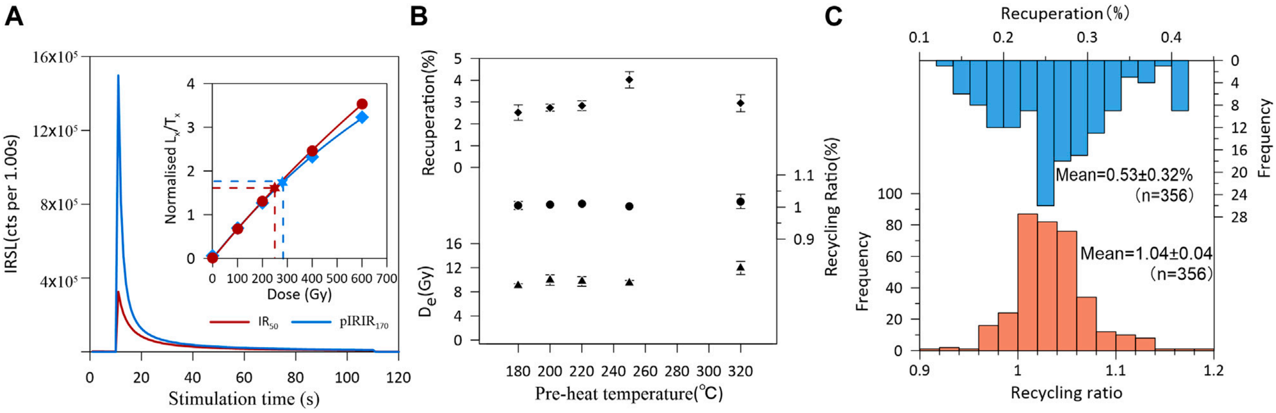

FIGURE 4
(A) Typical IR_{50} and $pIRIR_{170}$ decay curves and corresponding growth curves (inset) from a representative sample (LGN-286); **(B)** D_e plateau of pIRIR signals at different preheat and stimulation temperatures for sample LGN-302; **(C)** summarized recuperation (top) and recycling ratios (bottom) of $pIRIR_{170}$ signal from all 49 samples.

225°C IRSL with preheating at 250°C. The same preheat conditions were applied prior to the measurements of the natural and/or regenerative dose as well as the test dose. At the start and the end of each IRSL measurement, discs were held at the stimulation temperature without stimulating with IR (10 s for IR_{50} and pIRIR) to minimize any thermally stimulated signal. The integrated signal intensity over the initial 10 s of the signal minus a background of the last 40 s was used.

To assess the performance of the chosen measurement condition, dose recovery, fading, and residual tests were performed using eleven representative samples with different age ranges. Natural aliquots were bleached for 4 h in a Hönle UVACUBE 400 solar simulator prior to the tests. For the dose recovery test, the bleached aliquots were administered a beta dose approximately equivalent to the expected natural D_e of each sample. The anomalous fading rate (g-value) of pIRIR was measured using the method described by Auclair et al. (2003). In the test measurements, 3 to 4 aliquots were measured for each data point. Finally, 6–12 aliquots were measured at the chosen measurement condition ($pIRIR_{170}$) to calculate the D_e for all samples.

Radionuclide concentrations were determined by a combination of ICP-MS (for U and Th) and ICP-AES (for K) at Chang'an University (Xi'an, China). The conversion factors from the study by Guérin et al. (2011) were applied to convert the radionuclide concentrations to dose rate. Water contents were set to 10 ± 5% for aeolian sand and 20 ± 10% for palaeosol samples, based on the average measured *in situ* water content after sampling. The beta attenuation factors from the study by Mejdahl (1979) were applied and an a-value of 0.09 ± 0.02 was adopted (Balescu and Lamothe, 1994). Cosmic ray contributions were considered using the equations of Prescott and Hutton (1994). For the internal β-dose rate, K concentration of 12.5 ± 0.5% (Huntley and Baril, 1997) and Rb content of 400 μg/g (according to Huntley and Hancock, 2001) were assumed.

3.3 Grain size measurement

The grain size distributions of six representative samples from each unit were determined to aid a better understanding of their sedimentary characteristics. The grain size analysis was conducted by a Malvern 2000 laser particle size analyzer with a range of 0.02 to 2000 μm at Nanjing Institute of Geography and Limnology, Chinese Academy of Sciences. About 0.4–1.0 g material was used for each sample and pretreated by adding H_2O_2 and HCl to remove organic matter, and carbonate, and then were dispersed with 10% $(NaPO_3)_6$ on an ultrasonic treatment before grain size measurement (Liu et al., 2016).

4 Results and discussion

4.1 Luminescence characteristics and ages

Typical decay and dose–response curves for both natural IR_{50} and the following $pIRIR_{170}$ signals of sample LGN-286 are shown in Figure 4A. The growth curves can be well fitted using the single saturation exponential. All aliquots for the test measurements and D_e determination could pass the rejection criteria of 10% for the recycling error, 5% for the recuperation, and 15% for the test dose error. The pIRIR D_e plateau of sample LGN-302 is shown in Figure 4B. D_es showed no clear temperature dependency for all preheat and stimulation temperatures except that at 320°C. The recycling ratios are within 10% of unity, while the recuperations

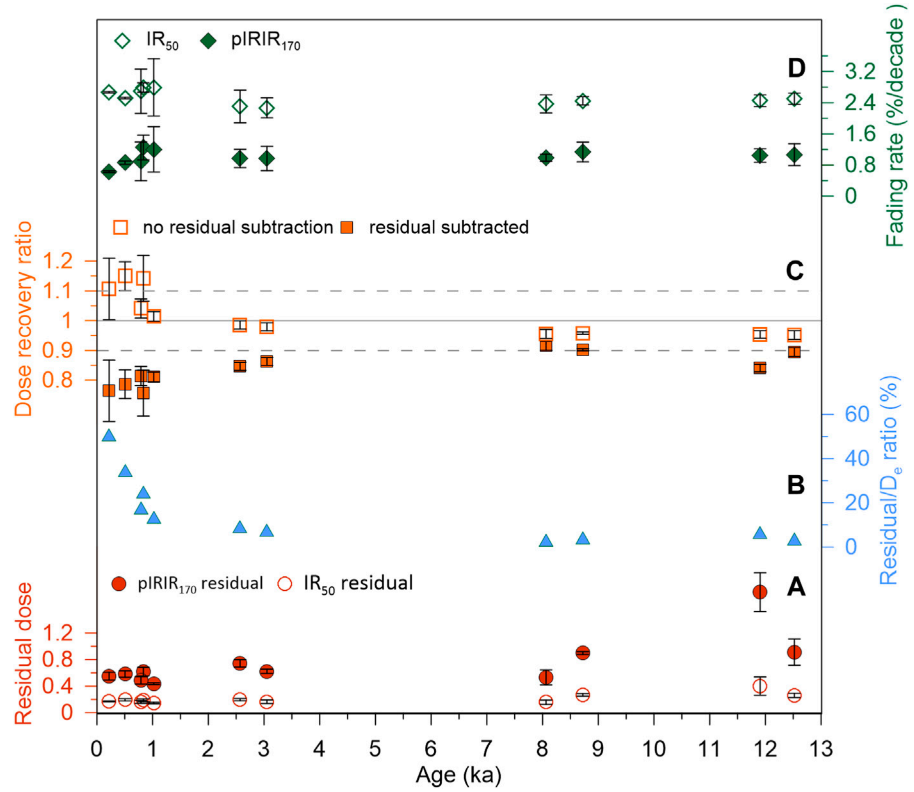

FIGURE 5
Residual dose, dose recovery ratio, and fading rate of eleven selected samples with different ages. **(A)** Residual dose of pIRIR$_{170}$ and IR$_{50}$ signals; **(B)** residual to D$_e$ ratio of pIRIR$_{170}$ signal; **(C)** the results of dose recovery test, the filled circles show the residual subtracted dose recovery ratios, the open circles show the value without residual subtraction; and **(D)** fading rates of IR$_{50}$ and pIRIR$_{170}$ signals measured in the same pIRIR$_{170}$ protocol.

are generally lower than 5% for all preheat temperatures. As a result, we selected the pIRIR$_{170}$ protocol for the D$_e$ determination. The average recycling ratio and recuperation of pIRIR$_{170}$ for all samples are 1.039 ± 0.037 and 0.53 ± 0.32%, respectively (Figure 4C). The D$_e$ distributions for six samples are displayed as radial plots (Supplementary Figure S1), and the D$_e$ values of these samples fall within narrow ranges since the number of aliquots is finite.

The primary assumption for luminescence dating is the sufficient resetting of the luminescence signals prior to deposition (Aitken, 1985). The feldspar pIRIR signal is considered to be more difficult to bleach than quartz OSL and the conventional IR signal that is stimulated at a lower temperature (50°C for instance) (Buylaert et al., 2012), and typically has a hard-to-bleach component (Kars et al., 2014). The bleachability is therefore of great importance in validating the pIRIR ages.

The residual doses remaining after 4 h bleaching are given in Figure 5A. There is a slight tendency for increasing residual with increasing equivalent dose. The residual dose measured for the IR$_{50}$ signal ranged between 0.14 and 0.40 Gy (0.04–0.1 ka in age), while that of the pIRIR$_{170}$ signal varied from ~0.4 to 2.4 Gy (0.1–0.7 ka in age), for the eleven selected samples. Such values are comparable with the previously published values (Thomsen et al., 2008; Buylaert et al., 2009). The ratio of the residual dose to the D$_e$s of pIRIR$_{170}$ signals for samples older than 1 ka lays in the range from 2% to 8% (Figure 5B), which is within the error of the ages, indicating that the contribution of the residual signal is negligible. For samples younger than 1 ka, although the ratio rose dramatically to 13–50%, the residual dose remained less than 0.6 Gy, equivalent to less than 0.2 ka. As a previous study suggested, bleaching in nature is likely more effective than the bleaching procedure in the laboratory, and the measured residual signal might be affected by thermal transfer (Stevens et al., 2011). Furthermore, the ages within the last millennium are not the major event of interest in the current study. The measured residual doses are not large enough to account for the dramatic variation in D$_e$ values, especially for samples older

TABLE 1 Summary of the radionuclide concentrations, total dose rates, grain size, equivalent doses, and age results for 49 K-feldspar pIRIR$_{170}$ dates from EBD1 and EBD2.

Section	Sample ID	Depth (cm)	U (ppm)	Th (ppm)	K (%)	Total dose rate (Gy/ka)	Grain size (μm)	pIRIR$_{170}$	Age (ka)
								D$_e$ (Gy)	
EBD1	LGN-266	30	1.37 ± 0.03	8.10 ± 0.07	1.71 ± 0.02	3.3 ± 0.1	150–200	1.7 ± 1.4	0.5 ± 0.4
EBD1	LGN-267	60	1.26 ± 0.02	6.62 ± 0.08	1.69 ± 0.00	3.1 ± 0.1	100–150	1.3 ± 0.9	0.4 ± 0.3
EBD1	LGN-268	90	1.40 ± 0.00	8.03 ± 0.06	1.74 ± 0.01	3.4 ± 0.1	150–200	1.2 ± 0.3	0.4 ± 0.1
EBD1	LGN-269	120	1.48 ± 0.03	8.30 ± 0.11	1.76 ± 0.02	3.4 ± 0.1	150–200	1.2 ± 0.1	0.4 ± 0.0
EBD1	LGN-270	150	1.38 ± 0.03	7.29 ± 0.15	1.59 ± 0.00	3.1 ± 0.1	150–200	1.5 ± 0.3	0.5 ± 0.1
EBD1	LGN-271	180	1.24 ± 0.02	6.86 ± 0.09	1.56 ± 0.01	3.0 ± 0.1	150–200	2.6 ± 0.7	0.9 ± 0.2
EBD1	LGN-272	210	1.59 ± 0.03	7.70 ± 0.07	1.78 ± 0.02	3.4 ± 0.1	150–200	2.7 ± 0.4	0.8 ± 0.1
EBD1	LGN-273	240	1.39 ± 0.01	7.37 ± 0.10	1.74 ± 0.02	3.2 ± 0.1	150-200	2.6 ± 0.1	0.8 ± 0.1
EBD1	LGN-274	270	1.43 ± 0.03	7.92 ± 0.11	1.72 ± 0.01	3.3 ± 0.1	150–200	3.1 ± 0.2	0.9 ± 0.1
EBD1	LGN-275	290	1.51 ± 0.05	7.32 ± 0.20	1.74 ± 0.03	3.3 ± 0.1	150–200	3.0 ± 0.2	0.9 ± 0.1
EBD1	LGN-276	310	1.68 ± 0.01	9.16 ± 0.04	1.94 ± 0.03	3.4 ± 0.2	150–250	3.5 ± 0.2	1.0 ± 0.1
EBD1	LGN-277	330	1.41 ± 0.01	7.77 ± 0.05	1.72 ± 0.02	3.1 ± 0.2	150–250	6.4 ± 0.2	2.1 ± 0.2
EBD1	LGN-278	350	1.30 ± 0.16	7.17 ± 0.87	1.65 ± 0.02	3.0 ± 0.2	150–250	7.2 ± 0.2	2.4 ± 0.2
EBD1	LGN-279	370	1.31 ± 0.01	6.96 ± 0.09	1.63 ± 0.02	3.1 ± 0.2	150–250	9.9 ± 1.5	3.2 ± 0.5
EBD1	LGN-280	390	1.19 ± 0.02	6.54 ± 0.06	1.49 ± 0.00	2.9 ± 0.1	150–200	9.1 ± 0.3	3.2 ± 0.2
EBD1	LGN-281	410	1.18 ± 0.03	6.93 ± 0.12	1.56 ± 0.01	3.0 ± 0.1	150–200	9.3 ± 0.2	3.1 ± 0.2
EBD1	LGN-282	430	1.24 ± 0.03	6.87 ± 0.22	1.57 ± 0.01	3.0 ± 0.2	150–250	10.8 ± 0.8	3.6 ± 0.3
EBD1	LGN-283	450	1.47 ± 0.03	8.10 ± 0.08	1.77 ± 0.01	3.1 ± 0.2	150–250	10.6 ± 0.3	3.4 ± 0.3
EBD1	LGN-284	470	1.64 ± 0.02	8.55 ± 0.11	1.73 ± 0.01	3.1 ± 0.2	150–250	11.2 ± 0.5	3.6 ± 0.3
EBD1	LGN-285	490	1.65 ± 0.03	8.94 ± 0.08	1.78 ± 0.04	3.2 ± 0.2	150–250	17.8 ± 0.8	5.6 ± 0.5
EBD1	LGN-286	510	1.31 ± 0.03	6.81 ± 0.07	1.63 ± 0.02	3.1 ± 0.2	150–250	25.0 ± 2.3	8.1 ± 0.9
EBD1	LGN-287	530	1.17 ± 0.03	6.52 ± 0.08	1.47 ± 0.01	2.8 ± 0.1	150–200	25.8 ± 0.8	9.1 ± 0.5
EBD1	LGN-288	550	1.15 ± 0.02	6.82 ± 0.13	1.39 ± 0.01	2.8 ± 0.1	150–200	26.9 ± 0.6	9.7 ± 0.5
EBD1	LGN-289	570	1.19 ± 0.02	6.46 ± 0.09	1.48 ± 0.00	2.8 ± 0.1	150–200	26.8 ± 0.3	9.5 ± 0.5
EBD1	LGN-290	590	1.28 ± 0.01	6.64 ± 0.04	1.90 ± 0.02	3.2 ± 0.1	150–200	28.8 ± 0.7	8.9 ± 0.4
EBD1	LGN-291	610	1.48 ± 0.05	6.98 ± 0.13	1.62 ± 0.02	3.0 ± 0.1	150–200	26.0 ± 0.5	8.5 ± 0.4

(Continued on following page)

TABLE 1 (*Continued*) Summary of the radionuclide concentrations, total dose rates, grain size, equivalent doses, and age results for 49 K-feldspar pIRIR$_{170}$ dates from EBD1 and EBD2.

Section	Sample ID	Depth (cm)	U (ppm)	Th (ppm)	K (%)	Total dose rate (Gy/ka)	Grain size (μm)	pIRIR$_{170}$	Age (ka)
								D$_e$ (Gy)	
EBD1	LGN-292	630	1.45 ± 0.02	9.48 ± 0.15	2.11 ± 0.01	3.5 ± 0.2	100–200	28.9 ± 0.6	8.2 ± 0.5
EBD2	LGN-293	20	1.56 ± 0.02	7.85 ± 0.09	1.86 ± 0.02	3.5 ± 0.1	150–200	0.8 ± 0.1	0.2 ± 0.0
EBD2	LGN-294	40	1.44 ± 0.02	6.65 ± 0.04	1.69 ± 0.04	3.3 ± 0.1	150–200	1.0 ± 0.1	0.3 ± 0.0
EBD2	LGN-295	60	1.55 ± 0.02	9.16 ± 0.08	1.84 ± 0.02	3.6 ± 0.1	150–200	1.4 ± 0.1	0.4 ± 0.0
EBD2	LGN-296	80	1.18 ± 0.03	6.48 ± 0.05	1.50 ± 0.02	3.0 ± 0.1	150–200	2.0 ± 0.6	0.7 ± 0.2
EBD2	LGN-297	100	1.67 ± 0.04	8.44 ± 0.10	1.77 ± 0.03	3.5 ± 0.1	150–200	1.4 ± 0.1	0.4 ± 0.0
EBD2	LGN-298	120	2.04 ± 0.03	8.83 ± 0.07	1.94 ± 0.02	3.7 ± 0.1	150–200	2.9 ± 0.2	0.8 ± 0.1
EBD2	LGN-299	140	1.21 ± 0.03	6.66 ± 0.06	1.65 ± 0.01	3.2 ± 0.2	150–250	5.8 ± 0.7	1.8 ± 0.3
EBD2	LGN-300	160	1.57 ± 0.03	7.79 ± 0.13	1.67 ± 0.02	3.3 ± 0.2	150–250	6.7 ± 0.7	2.0 ± 0.3
EBD2	LGN-301	180	1.37 ± 0.01	7.09 ± 0.06	1.67 ± 0.02	3.2 ± 0.3	100–250	7.7 ± 0.2	2.4 ± 0.2
EBD2	LGN-302	200	1.63 ± 0.03	9.04 ± 0.10	1.87 ± 0.03	3.5 ± 0.1	150–200	9.1 ± 0.4	2.6 ± 0.1
EBD2	LGN-303	210	1.81 ± 0.03	10.88 ± 0.08	2.07 ± 0.02	3.6 ± 0.2	150–250	10.1 ± 0.4	2.8 ± 0.2
EBD2	LGN-304	230	2.25 ± 0.04	12.55 ± 0.16	2.10 ± 0.02	3.8 ± 0.2	150–250	15.4 ± 1.8	4.0 ± 0.5
EBD2	LGN-305	250	2.14 ± 0.03	11.15 ± 0.13	1.92 ± 0.02	3.6 ± 0.2	150–250	32.6 ± 1.4	9.1 ± 0.7
EBD2	LGN-306	270	2.10 ± 0.03	11.13 ± 0.14	1.95 ± 0.00	3.6 ± 0.2	150–250	34.5 ± 1.1	9.6 ± 0.7
EBD2	LGN-307	290	0.93 ± 0.01	5.01 ± 0.03	1.15 ± 0.01	2.5 ± 0.1	150–200	30.4 ± 1.1	12.3 ± 0.8
EBD2	LGN-308	310	1.12 ± 0.01	4.50 ± 0.04	0.91 ± 0.01	2.3 ± 0.2	150–250	29.3 ± 1.6	12.5 ± 1.3
EBD2	LGN-309	330	1.06 ± 0.01	4.98 ± 0.06	0.98 ± 0.01	2.3 ± 0.2	100–200	28.7 ± 0.8	12.7 ± 1.2
EBD2	LGN-310	350	0.97 ± 0.01	4.81 ± 0.02	1.05 ± 0.01	2.4 ± 0.3	100–250	32.3 ± 0.9	13.7 ± 1.7
EBD2	LGN-311	370	1.55 ± 0.02	5.63 ± 0.07	2.11 ± 0.01	2.7 ± 0.2	100–200	35.3 ± 1.5	13.1 ± 1.1
EBD2	LGN-312	670	1.44 ± 0.01	7.13 ± 0.10	1.33 ± 0.03	2.8 ± 0.2	100–200	34.1 ± 1.2	12.0 ± 1.0
EBD2	LGN-313	720	1.41 ± 0.02	5.76 ± 0.04	1.29 ± 0.01	2.8 ± 0.2	100–200	32.9 ± 0.7	11.9 ± 0.9
EBD2	LGN-314	770	1.02 ± 0.01	4.71 ± 0.05	1.34 ± 0.03	2.5 ± 0.2	100–200	35.7 ± 1.2	14.1 ± 1.2

than 1 ka. Therefore, we consider the pIRIR$_{170}$ signal of the samples could be well bleached and it is not necessary to subtract the residual dose from the D$_e$s.

As shown in Figure 5C, dose recovery ratios are generally within 10% of unity before the residual subtraction, while the ratios for samples younger than 1 ka are all above the unity,

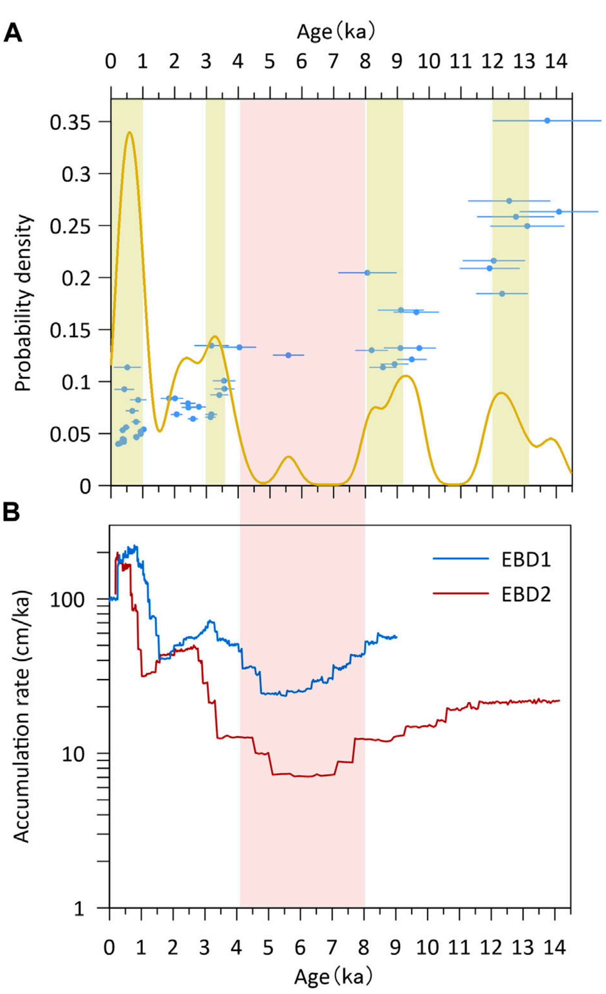

FIGURE 6
(A) Probability density plot of 49 luminescence ages; **(B)** the calculated accumulation rates of EBD1 (blue line) and EBD2 (red line) sections. The ruby red bar shows the lowest accumulation rate phase while the yellow bars denote the peaks of aeolian accumulation.

showing larger scatter in data. It is noteworthy that after residual subtraction, the dose recovery ratios decreased to below 0.9 for samples younger than 1 ka, owing to the high residual dose/D_e dose ratio. For relatively older samples, the performance of the dose recovery tests is overall acceptable, with a slightly underestimation tendency after residual dose subtraction.

Anomalous fading is a key issue affecting the reliability of feldspar IRSL signals (Wintle, 1973), potentially resulting in an overall age underestimation of the sediments. Previous studies have shown the pIRIR signal could significantly reduce the degree of anomalous fading and be more stable than the IRSL signal. We would expect $pIRIR_{170}$ to fade less than the IR_{50} signal. The fading rate of the selected eleven samples ranged from 0.63 to 1.25%/decade with an average of 1.00 ± 0.17%/decade (n = 44) for the $pIRIR_{170}$ signal (Figure 5D), which is remarkably smaller than the average value obtained for the corresponding IR_{50} signal (2.53 ± 0.18%/decade). This pattern is consistent with the observations of previous studies (Thomsen et al., 2008; Kars et al., 2014). No clear correlation between the fading rates and ages was observed for both IR_{50} and $pIRIR_{170}$ signals. The low values demonstrate that there is minimal fading of the $pIRIR_{170}$ signal in these samples. Since the fading rates of less than ca. 1.5% have been considered laboratory artifacts (Vasiliniuc et al., 2011; Buylaert et al., 2012; Long et al., 2017; Roberts et al., 2018), no fading correction is conducted for all samples.

A summary of the radionuclide concentrations, dose rates, equivalent doses, and age results for all 49 samples is listed in Table 1. The total dose rates varied from 2.3 to 3.8 Gy/ka. The palaeosol generally has a higher dose rate than the aeolian sand. This is because the U and Th tend to enrich more in silts than sands (Peng et al., 2022), resulting in relatively larger dose rates in soil layers. The $pIRIR_{170}$ D_es ranged between 0.8 ± 0.1 Gy and 35.7 ± 1.2 Gy. The corresponding ages fall into the range between 0.2 ± 0.0 ka and 14.1 ± 1.2 ka, generally following the stratigraphical order from the bottom to the top (Figure 3). The chronostratigraphy fully covers the Late Glacial and Holocene periods, demonstrating that the aeolian deposition in the study area commenced at least since the late Glacial and was interrupted by palaeosol formation in the middle of the Holocene (Figure 3).

4.2 Grain size

Figure 3 shows the typical grain size distribution curve of each unit. The grain size distributions of aeolian sand were generally unimodal, while the palaeosol layer and the transition layer (from soil to aeolian sand) showed bimodal distribution with a fine sand and coarse silt component. The curve of the palaeosol shows a broad peak at ~10 μm and a major peak at ~100 μm. The grain size distributions of the transitional layer were similar to those of the palaeosol layer but contained more sand fraction. The grain size data are generally in agreement with our field observation.

4.3 Interpretation of luminescence dates and reconstruction of Holocene aeolian activities

For aeolian sedimentary archives, age gaps may represent a lack of net accumulation due to a reduction in sediment deposition (Long et al., 2017) and/or an increase in the reworking or erosion of previously deposited units (Stevens et al., 2018). For the aeolian sand sedimentary sequences in this study, we consider that the extremely low net deposition during the middle Holocene may reflect dune stability with dense

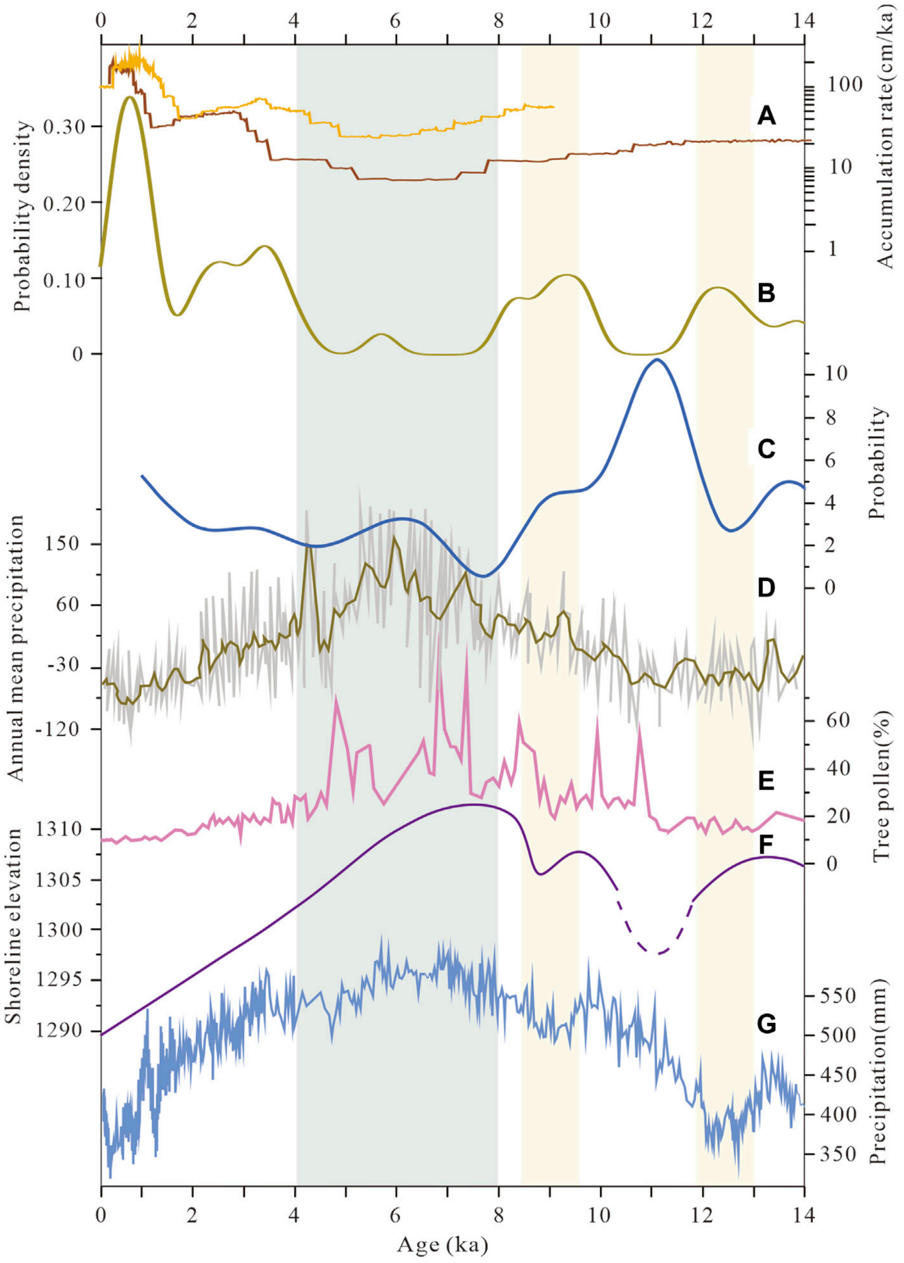

FIGURE 7
The aeolian–palaeosol records in the current study and other records in the adjacent area in NETP. **(A)** Accumulation rates of EBD1 (yellow line) and EBD2 (red line), and **(B)** PDF of all luminescence ages of EBD1 and EBD2; **(C)** PDF of the previously published luminescence ages of aeolian sand over the NETP (Chen et al., 2016); **(D)** quantitative reconstructed precipitation based on pollen data from Qinghai Lake (Li et al., 2017); **(E)** tree pollen percentages from Lake Dalianhai (Cheng et al., 2013); **(F)** water level history of Baijian Lake (Long et al., 2012); and **(G)** EASM precipitation variation record from Lake Gonghai (Chen et al., 2015).

vegetation cover due to climate forcing on a large regional scale. Wind erosion might have also played a role, but not the major one. The least sediment accumulation revealed in our records is broadly comparable with the other aeolian records over the entire NETP. For instance, Chen et al. (2016) compiled a large number of OSL ages of aeolian sand sections from NETP with a probability density function (PDF) plot, showing the lowest PDF values as an implication of very weak aeolian activity during the middle Holocene. Based on high-resolution OSL dating of a mega dune in the eastern Qinghai Lake basin, Yang et al. (2019) reported a similar low accumulation rate accompanied by palaeosol formation during the period of 6–3 ka. Such low accumulation rates in the middle Holocene have also been found from a loess sequence from the west of the Qinghai Lake Basin, where the least accumulation stage was dated to the period of ~7–4 ka based on high-resolution OSL sampling at a vertical interval of 15 cm (ChongYi et al., 2019). Furthermore, from the southern bank of the Qinghai Lake, a chronological gap of ~4 ka (between 6 and 2 ka) was revealed in the loess profile based on high-resolution OSL sampling (Zhang et al., 2022). Overall, both loess and dune sand sequences have shown a consistent low deposition rate during the middle Holocene in the NETP.

The grain size distributions revealed that the mode of sand (>100 μm) fraction continuously existed in the whole sedimentary sequence. Notwithstanding the effect of the sampling strategy (Leighton et al., 2013), the frequency of all ages may suggest sedimentary continuity with particle size fraction of >100 μm from both dune sediments and palaeosols, which can be an indicator of aeolian activities (Long et al., 2017). The PDF plot of all 49 luminescence ages is shown in Figure 6A, which overall suggests three different epochs of aeolian activity variations during the last 14 ka: 1) a highly intensified aeolian activity stage between 14 and 8 ka (late glacial and early Holocene) with two dune sand accumulation peaks at 13–12 ka and 9–8 ka; 2) a period of significantly decreased aeolian activity between 8 and 3.5 ka (middle Holocene) when the soil formation prevailed, and particularly very few luminescence dates fall in this period, which may imply the strongest pedogenesis intensity and the least aeolian activity; and 3) increasing aeolian activity since ~3.5 ka (late Holocene) with two peaks around ~3 ka and 0.8 ka. The accumulation rate of the aeolian sand/palaeosol sequence may also reveal changes in aeolian activity (Yang et al., 2013). In general, a higher deposition rate is expected for the aeolian sediments than for the soil formation period. We use all OSL ages to construct the Bacon age-depth model and then recover the history of sedimentation rate (SR) changes; the SRs of two sequences (EBD1 and EBD2) show a very similar pattern, which can be generally divided into three stages (Figure 6B): relatively faster SRs during ~14–8 ka and after ~4 ka corresponding to two states with strengthened aeolian activities (Figure 6A), and a very low accumulation rate during the middle Holocene (~8–4 ka) was recognized.

4.4 Inference of the past moisture variations and regional comparison

Aeolian accumulation and soil formation have long been associated with environmental changes. The aeolian sand accumulation indicates the sand mobilization with minimal vegetation cover and hence dry conditions, while the development of palaeosol indicates the dune stabilization with vegetation development and thus a relatively humid environment (Lu et al., 2011; Long et al., 2017; Yang et al., 2019). Therefore, according to the aeolian sand accumulation history inferred from the investigated dune field, we can infer the late Glacial and Holocene moisture variation in the alpine basin in the southeast Qilian Mountains. This can be roughly divided into three stages: 1) the arid stage during the late glacial and early Holocene (14–8 ka), which could be characterized by sparse vegetation and sand dune mobility; 2) the wettest period between ~8 ka and ~4 ka with the strongest pedogenesis; and 3) the following arid conditions during the late Holocene (Figures 7A,B). In addition, four drought events on the millennial time scales can be recognized that are indicated by the intensified aeolian activities at 13–12 ka, 9.5–8.5 ka, ~3.5 ka, and ~1 ka.

Although the connection between climate and sand dune accumulation might not be straightforward, the transition between the sand dune accumulation and soil formation in the same sedimentary sequence could be driven by the regional effective moisture, which is mainly determined by the balance of precipitation and potential evaporation (Stauch et al., 2012; Qiang et al., 2013, 2016; Stauch, 2015). In order to further investigate the Holocene moisture evolution pattern in the NETP and its influencing mechanisms, we compared our records from the Babao River drainage (Figures 7A,B) with other moisture variation archives from the adjacent areas. Our records were generally consistent with different moisture records such as tree pollen (Cheng et al., 2013; Li et al., 2017), lake level (Long et al., 2012), and OSL chronologies of aeolian sands (Chen et al., 2020), as well as the well-dated monsoon precipitation record (Chen et al., 2016) on a different time scale.

It is obvious that the phase with the minimum sand accumulation in the Babao River during the middle Holocene is consistent with the low frequency of OSL ages (Figure 7C) compiled from dune sediment samples over the entire NETP (Chen et al., 2016). This suggests that the limited aeolian activity of 8–4 ka in the Babao River drainage basin may reflect a contemporary event on the regional scale. The moisture optimum during the middle Holocene can be further confirmed by a set of robust lake records from the adjacent areas. The pollen-based quantitative reconstruction from Qinghai Lake shows that the wetness increased from the early Holocene to the middle Holocene and culminated during the middle Holocene (Figure 7D and Figure 1A ①; Li et al., 2017). Another pollen record from Dalianhai, a lake to the south of Lake Qinghai, demonstrated the most tree concentrations as an indication of optimum conditions during the middle Holocene (Figure 7E and Figure 1A ②; Cheng et al., 2013). Water levels of Baijian Lake from Tengger Desert show that the lake sustained a high stand from ~8 ka to ~5 ka (Figure 7F; Long et al., 2012), also suggesting the similarity of the moisture variation pattern for NETP and its foreland desert areas. It should be noted that all these moisture variation records show a similar pattern to the East Asian summer monsoon (EASM) precipitation history, inferred from pollen-based quantitative reconstruction from

Gonghai Lake, northern China (Figure 7G and Figure 1A ④; Chen et al., 2015). In addition, the intensified aeolian activities dominated during 13–12 ka and 9.5–8.5 ka in our record, suggesting two dry events on the millennial time scales. These dry events could correspond to the weakened EASM during the Younger Dryas (YD) event and the ~9 ka event with decreased precipitation from the late glacial to early Holocene (Figure 7G, Chen et al., 2015). Thus, we deduce that the moisture variations in NETP should be mainly regulated by the EASM precipitations over both orbital and millennial time scales.

5 Conclusion

Two aeolian sand/palaeosol sequences were obtained from the Babao River Basin in the southeast of the Qilian Mountains in the NETP. Based on the high-resolution K-feldspar pIRIR_{170} dating of 49 samples, we set up a robust chronology for the sand dune accumulation. The reconstructed aeolian activities can be divided into three stages, namely, aeolian sand accumulation prevailed during 14–8 ka, the soil development and limited aeolian activity between 8 ka and 4 ka, and the reactivated aeolian processes after 4 ka. Such aeolian activities indicated moisture optimum in the middle Holocene but relatively dry conditions dominated the late glacial to early Holocene and late Holocene periods, together with several drought events at millennial time scales. The regional comparison suggested the EASM intensity (precipitation) was likely the dominant forcing factor for the aeolian activity and moisture conditions over the NETP.

Data availability statement

The original contributions presented in the study are included in the article/Supplementary Material; further inquiries can be directed to the corresponding authors.

Author contributions

JZ and HL contributed to the conception and design of the study. NY and YC conducted the luminescence dating work in the lab. NY wrote the first draft of the manuscript. JZ and HL rewrote part of the manuscript. All authors contributed to manuscript revision, and read and approved the submitted version.

Funding

This research was supported by the Strategic Priority Research Program of the Chinese Academy of Sciences (No. XDB40010200), the National Natural Science Foundation of China (No. 41977381), Youth Innovation Promotion Association, CAS (grant No. Y201959), and the State Key Laboratory of Loess and Quaternary Geology, Institute of Earth Environment, CAS (grant No. SKLLQG2105 to JZ).

Acknowledgments

The authors thank two reviewers for their constructive comments that improved the quality of this manuscript.

Conflict of interest

The authors declare that the research was conducted in the absence of any commercial or financial relationships that could be construed as a potential conflict of interest.

Publisher's note

Supplementary material

The Supplementary Material for this article can be found online at: https://www.frontiersin.org/articles/10.3389/feart.2022.939887/full#supplementary-material

References

Aitken, M. J. (1985). *Thermoluminescence dating*. London: Academic Press.

An, Z. S., Colman, S. M., Zhou, W. J., Li, X. Q., Brown, E. T., Jull, A. J. T., et al. (2012). Interplay between the westerlies and Asian monsoon recorded in Lake Qinghai sediments since 32 ka. *Sci. Rep.* 2, 619. doi:10.1038/srep00619

An, Z. S., Porter, S. C., Kutzbach, J. E., Wu, X. H., Wang, S. M., Liu, X. D., et al. (2000). Asynchronous Holocene optimum of the east asian monsoon. *Quat. Sci. Rev.* 19, 743–762. doi:10.1016/s0277-3791(99)00031-1

Auclair, M., Lamothe, M., and Huot, S. (2003). Measurement of anomalous fading for feldspar IRSL using SAR. *Radiat. Meas.* 37 (4–5), 487–492. doi:10.1016/s1350-4487(03)00018-0

Balescu, S., and Lamothe, M. (1994). Comparison of TL and IRSL age estimates of feldspar coarse grains from waterlain sediments. *Quat. Sci. Rev.* 13, 437–444. doi:10.1016/0277-3791(94)90056-6

Bond, G., Kromer, B., Beer, J., Muscheler, R., Evans, M. N., Showers, W., et al. (2001). Persistent solar influence on north Atlantic climate during the Holocene. *Science* 294, 2130–2136. doi:10.1126/science.1065680

Buylaert, J. P., Jain, M., Murray, A. S., Thomsen, K. J., Thiel, C., and Sohbati, R. (2012). A robust feldspar luminescence dating method for Middle and Late Pleistocene sediments. *Boreas* 41, 435–451. doi:10.1111/j.1502-3885.2012.00248.x

Buylaert, J. P., Murray, A. S., Thomsen, K. J., and Jain, M. (2009). Testing the potential of an elevated temperature IRSL signal from K-feldspar. *Radiat. Meas.* 44, 560–565. doi:10.1016/j.radmeas.2009.02.007

Chen, F. H., Zhang, J. F., Liu, J. B., Cao, X. Y., Hou, J. Z., Zhu, L. P., et al. (2020). Climate change, vegetation history, and landscape responses on the Tibetan plateau during the Holocene: A comprehensive review. *Quat. Sci. Rev.* 243 (1), 106444. doi:10.1016/j.quascirev.2020.106444

Chen, F., Wu, D., Chen, J., Zhou, A., Yu, J., Shen, J., et al. (2016). Holocene moisture and east Asian summer monsoon evolution in the northeastern Tibetan plateau recorded by Lake Qinghai and its environs: A review of conflicting proxies. *Quat. Sci. Rev.* 154, 111–129. doi:10.1016/j.quascirev.2016.10.021

Chen, F., Xu, Q., Chen, J., Birks, H. J., Liu, J., Zhang, S., et al. (2015). East Asian summer monsoon precipitation variability since the last deglaciation. *Sci. Rep.* 5, 11186. doi:10.1038/srep11186

Cheng, B., Chen, F., and Zhang, J. (2013). Palaeovegetational and palaeoenvironmental changes since the last deglacial in Gonghe Basin, northeast Tibetan Plateau. *J. Geogr. Sci.* 23 (1), 136–146. doi:10.1007/s11442-013-0999-5

Cheng, G. D., Li, X., Zhao, W. Z., Xu, Z. M., Feng, Q., Xiao, S. C., et al. (2014). Integrated study of the water-ecosystem-economy in the Heihe River basin. *Natl. Sci. Rev.* 1 (3), 413–428. doi:10.1093/nsr/nwu017

ChongYi, E., Jing, Z., ZongYan, C., YongJuan, S., YaJuan, Z., Ping, L., et al. (2019). High resolution OSL dating of aeolian activity at Qinghai Lake, northeast Tibetan plateau. *Catena* 183, 104180. doi:10.1016/j.catena.2019.104180

Guérin, G., Mercier, N., and Adamiec, G. (2011). Dose-rate conversion factors: Update. *Anc. TL* 29, 5–8.

Hou, J., D'Andrea, W. J., and Liu, Z. (2012). The influence of 14C reservoir age on interpretation of paleolimnological records from the Tibetan Plateau. *Quat. Sci. Rev.* 48, 67–79. doi:10.1016/j.quascirev.2012.06.008

Huntley, D. J., and Baril, M. R. (1997). The K content of the K-feldspars being measured in optical dating or in thermoluminescence dating. *Anc. TL* 15, 11–13.

Huntley, D. J., and Hancock, R. G. V. (2001). The Rb contents of the K-feldspars being measured in optical dating. *Anc. TL* 19, 43–46.

Jin, Z., An, Z., Yu, J., Li, F., and Zhang, F. (2015). Lake Qinghai sediment geochemistry linked to hydroclimate variability since the last glacial. *Quat. Sci. Rev.* 122, 63–73. doi:10.1016/j.quascirev.2015.05.015

Kang, S., Du, J., Wang, N., Dong, J., Wang, D., Wang, X., et al. (2020). Early Holocene weakening and mid- to late Holocene strengthening of the East Asian winter monsoon. *Geology* 48 (11), 1043–1047. doi:10.1130/g47621.1

Kars, R. H., Reimann, T., and Wallinga, J. (2014). Are feldspar SAR protocols appropriate for post-IR IRSL dating? *Quat. Geochronol.* 22, 126–136. doi:10.1016/j.quageo.2014.04.001

Leighton, C. L., Bailey, R. M., and Thomas, D. S. G. (2013). The utility of desert sand dunes as quaternary chronostratigraphic archives: Evidence from the northeast rub' al Khali. *Quat. Sci. Rev.* 78, 303–318. doi:10.1016/j.quascirev.2013.04.016

Li, G., Zhang, H., Liu, X., Yang, H., Wang, X., Zhang, X., et al. (2020). Paleoclimatic changes and modulation of East Asian summer monsoon by high-latitude forcing over the last 130, 000 years as revealed by independently dated loess-paleosol sequences on the NE Tibetan Plateau. *Quat. Sci. Rev.* 237, 106283. doi:10.1016/j.quascirev.2020.106283

Li, J. Y., Dodson, J., Yan, H., Cheng, B., Zhang, X. J., Xu, Q. H., et al. (2017). Quantitative precipitation estimates for the northeastern Qinghai-Tibetan Plateau over the last 18, 000 years. *J. Geophys. Res. Atmos.* 122, 5132–5143. doi:10.1002/2016jd026333

Lister, G. S., Kelts, K., Chen, K. Z., Jun-Qing, Y., and Niessena, F. (1991). Lake Qinghai, China: Closed- basin lake levels and the oxygen isotope record for ostracoda since the latest pleistocene. *Palaeogeogr. Palaeoclimatol. Palaeoecol.* 84, 141–162. doi:10.1016/0031-0182(91)90041-O

Liu, X., Colman, S. M., Brown, E. T., An, Z., Zhou, W., Jull, A. J. T., et al. (2014). A climate threshold at the eastern edge of the Tibetan plateau. *Geophys. Res. Lett.* 41 (15), 5598–5604. doi:10.1002/2014gl060833

Liu, X., Cong, L., An, F., Miao, X., and E, C. (2019). Downwind aeolian sediment accumulations associated with lake-level variations of the Qinghai lake during the Holocene, northeastern Qinghai–Tibetan plateau. *Environ. Earth Sci.* 78 (1), 19. doi:10.1007/s12665-018-8025-y

Liu, X., Herzschuh, U., Shen, J., Jiang, Q., and Xiao, X. (2008). Holocene environmental and climatic changes inferred from wulungu lake in northern xinjiang, China. *Quat. Res.* 70, 412–425. doi:10.1016/j.yqres.2008.06.005

Liu, X., Vandenberghe, J., An, Z., Li, Y., Jin, Z., Dong, J., et al. (2016). Grain size of Lake Qinghai sediments: Implications for riverine input and Holocene monsoon variability. *Palaeogeogr. Palaeoclimatol. Palaeoecol.* 449, 41–51. doi:10.1016/j.palaeo.2016.02.005

Long, H., Fuchs, M., Yang, L., and Cheng, H. (2016). Abrupt sand-dune accumulation at the Northeastern margin of the Tibetan Plateau challenges the wet MIS3a inferred from numerous lake-highstands. *Sci. Rep.* 6 (1), 25820. doi:10.1038/srep25820

Long, H., Lai, Z., Fuchs, M., Zhang, J., and Li, Y. (2012). Timing of Late Quaternary palaeolake evolution in Tengger Desert of northern China and its possible forcing mechanisms. *Glob. Planet. Change* 92-93, 119–129. doi:10.1016/j.gloplacha.2012.05.014

Long, H., Lai, Z., Wang, N., and Zhang, J. (2011). A combined luminescence and radiocarbon dating study of Holocene lacustrine sediments from arid northern China. *Quat. Geochronol.* 6 (1), 1–9. doi:10.1016/j.quageo.2010.06.001

Long, H., Shen, J., Chen, J., Tsukamoto, S., Yang, L., Cheng, H., et al. (2017). Holocene moisture variations over the arid central Asia revealed by a comprehensive sand-dune record from the central Tian Shan, NW China. *Quat. Sci. Rev.* 174, 13–32. doi:10.1016/j.quascirev.2017.08.024

Long, H., Shen, J., Wang, Y., Gao, L., and Frechen, M. (2015). High resolution OSL dating of a late quaternary sequence from xingkai lake (NE asia): Chronological challenge of the "MIS3a mega-paleolake" hypothesis in China. *Earth Planet. Sci. Lett.* 428, 281–292. doi:10.1016/j.epsl.2015.07.003

Lu, H., Mason, J. A., Stevens, T., Zhou, Y., Yi, S., and Miao, X. (2011). Response of surface processes to climatic change in the dunefields and Loess Plateau of North China during the late Quaternary. *Earth Surf. Process. Landforms* 36 (12), 1590–1603. doi:10.1002/esp.2168

Mayewski, P. A., Rohling, E. E., Curt Stager, J., Karl´en, W., Maasch, K. A., Meeker, L. D., et al. (2004). Holocene climate variability. *Quat. Res.* 62, 243–255. doi:10.1016/j.yqres.2004.07.001

Mejdahl, V. (1979). Thermoluminescence dating: Beta-dose attenuation in quartz grains. *Archaeometry* 21, 61–72. doi:10.1111/j.1475-4754.1979.tb00241.x

Mischke, S., Weynell, M., Zhang, C., and Wiechert, U. (2013). Spatial variability of 14C reservoir effects in Tibetan Plateau lakes. *Quat. Int.* 313-314, 147–155. doi:10.1016/j.quaint.2013.01.030

Niu, Z, R., and An, D. (2013). Change characteristics of temperature, precipitation and evaporation in upper and middle reaches of eastern Heihe River basin in recent 60 years. *J. China Hydro* 33, 85–89. In Chinese with English abstract.

Peng, Z., Wang, X. L., Yin, G. M., Adamiec, G., Du, J. H., Zhao, H., et al. (2022). Accumulation of aeolian sediments around the Tengger Desert during the late Quaternary and its implications on interpreting chronostratigraphic records from drylands in north China. *Quat. Sci. Rev.* 275, 107288. doi:10.1016/j.quascirev.2021.107288

Prescott, J. R., and Hutton, J. T. (1994). Cosmic ray contributions to dose rates for luminescence and ESR dating: Large depths and long-term time variations. *Radiat. Meas.* 23, 497–500. doi:10.1016/1350-4487(94)90086-8

Qiang, M. R., Chen, F. H., Song, L., Liu, X. X., Li, M. Z., and Wang, Q. (2013). Late quaternary aeolian activity in Gonghe Basin, northeastern Qinghai-Tibetan plateau, China. *Quat. Res.* 79, 403–412. doi:10.1016/j.yqres.2013.03.003

Qiang, M. R., Jin, Y. X., Liu, X. X., Song, L., Li, H., Li, F. S., et al. (2016). Late pleistocene and Holocene aeolian sedimentation in Gonghe Basin, northeastern Qinghai-Tibetan plateau: Variability, processes, and climatic implications. *Quat. Sci. Rev.* 132, 57–73. doi:10.1016/j.quascirev.2015.11.010

Roberts, H. M., Bryant, C. L., Huws, D. G., and Lam, H. F. (2018). Generating long chronologies for lacustrine sediments using luminescence dating: A 250, 000 year record from Lake tana, Ethiopia. *Quat. Sci. Rev.* 202, 66–77. doi:10.1016/j.quascirev.2018.10.037

Stauch, G. (2015). Geomorphological and palaeoclimate dynamics recorded by the formation of aeolian archives on the Tibetan Plateau. *Earth. Sci. Rev.* 150, 393–408. doi:10.1016/j.earscirev.2015.08.009

Stauch, G., IJmaker, J., Potsch, S., Zhao, H., Hilgers, A., Diekmann, B., et al. (2012). Aeolian sediments on the north-eastern Tibetan plateau. *Quat. Sci. Rev.* 57, 71–84. doi:10.1016/j.quascirev.2012.10.001

Stevens, S., Just, E., Cordes, R., Brooks, R., and Serfass, T. (2011). The influence of habitat quality on the detection of river otter (Lontra canadensis) latrines near bridges. *Am. Midl. Nat.* 166, 435–445. doi:10.1674/0003-0031-166.2.435

Stevens, T., Buylaert, J. P., Thiel, C., Újv´ari, G., Yi, S., Murray, A. S., et al. (2018). Ice-volume-forced erosion of the Chinese Loess Plateau global Quaternary stratotype site. *Nat. Commun.* 9, 983. doi:10.1038/s41467-018-03329-2

Telfer, M. W., and Thomas, D. S. G. (2007). Late quaternary linear dune accumulation and chronostratigraphy of the southwestern kalahari: Implications for aeolian palaeoclimatic reconstructions and predictions of future dynamics. *Quat. Sci. Rev.* 26 (19-21), 2617–2630. doi:10.1016/j.quascirev.2007.07.006

Thomas, E. K., Huang, Y., Clemens, S. C., Colman, S. M., Morrill, C., Wegener, P., et al. (2016). Changes in dominant moisture sources and the consequences for hydroclimate on the northeastern Tibetan Plateau during the past 32 kyr. *Quat. Sci. Rev.* 131, 157–167. doi:10.1016/j.quascirev.2015.11.003

Thomsen, K. J., Murray, A. S., Jain, M., and Bøtter-Jensen, L. (2008). Laboratory fading rates of various luminescence signals from feldspar-rich sediment extracts. *Radiat. Meas.* 43 (9), 1474–1486. doi:10.1016/j.radmeas.2008.06.002

Vasiliniuc, S., Timar Gabor, A., Vandenberghe, D. A. G., Panaiotu, C. G., Begy, R. C. S., and Cosma, C. (2011). A high resolution optical dating study of the Mostistea loess–palaeosol sequence (SE Romania) using sand–sized quartz. *Geochronometria* 38, 34–41. doi:10.2478/s13386-011-0007-8

Wei, K., and Gasse, F. (1999). Oxygen isotopes in lacustrine carbonates of west China revisited: Implications for post glacial changes in summer monsoon circulation. *Quat. Sci. Rev.* 18, 1315–1334. doi:10.1016/s0277-3791(98)00115-2

Wintle, A. G. (1973). Anomalous fading of thermoluminescence in mineral samples. *Nature* 245, 143–144. doi:10.1038/245143a0

Yang, L., Long, H., Cheng, H., He, Z., and Hu, G. (2019). OSL dating of a mega-dune in the eastern Lake Qinghai basin (northeastern Tibetan Plateau) and its implications for Holocene aeolian activities. *Quat. Geochronol.* 49, 165–171. doi:10.1016/j.quageo.2018.02.005

Yang, X., Wang, X., Liu, Z., Li, H., Ren, X., Zhang, D., et al. (2013). Initiation and variation of the dune fields in semi-arid China – With a special reference to the hunshandake sandy land, inner Mongolia. *Quat. Sci. Rev.* 78, 369–380. doi:10.1016/j.quascirev.2013.02.006

Zhang, J. R., Liu, Q., Yang, L. H., Cheng, H. Y., Cai, Y., and Long, H. (2022). Regional hydroclimates regulate the Holocene aeolian accumulation processes of the Qinghai Lake basin on the northeastern Tibetan plateau. *Catena* 210, 105866. doi:10.1016/j.catena.2021.105866